# optica

# Mapping complex mode volumes with cavity perturbation theory

K. G. Cognée,[1,2] W. Yan,[1] F. La China,[3] D. Balestri,[3] F. Intonti,[3] M. Gurioli,[3] A. F. Koenderink,[2] and P. Lalanne[1,*]

[1]LP2N, Institut d'Optique, CNRS, Univ. Bordeaux, Talence, 33400, France
[2]Center for Nanophotonics, AMOLF, Science Park 104, 1098XG, Amsterdam, The Netherlands
[3]LENS, University of Florence, Sesto Fiorentino, 50019, Italy
*Corresponding author: philippe.lalanne@institutoptique.fr

**Microcavities and nanoresonators are characterized by their quality factors ($Q$) and mode volumes ($V$). While $Q$ is unambiguously defined, there are still questions on $V$ and, in particular, on its complex-valued character, whose imaginary part is linked to the non-Hermitian nature of open systems. Helped by cavity perturbation theory and near-field experimental data, we clarify the physics captured by the imaginary part of $V$ and show how a mapping of the spatial distribution of both the real and imaginary parts can be directly inferred from perturbation measurements. This result shows that the mathematically abstract complex mode $V$, in fact, is directly observable.** © 2019

Predicting how the presence of a tiny foreign object near a resonant optical cavity perturbs the optical response is a classical problem in electromagnetics, with important implications spanning from the radio-frequency domain to present-day nano-optics. The perturbation results in a modification $\Delta\tilde{\omega}$ of the initial complex resonance frequency $\tilde{\omega} \equiv \omega_0 + i\gamma_0/2$ of the unperturbed cavity mode, $\text{Re}(\Delta\tilde{\omega})$ and $\text{Im}(\Delta\tilde{\omega})$, respectively, representing the frequency shift and linewidth change. For a tiny perturbation quantified by a dipolar polarizability $\alpha$ (assumed to be small and isotropic) and placed at $\mathbf{r}_0$, $\Delta\tilde{\omega}$ usually reads as

$$\frac{\Delta\tilde{\omega}}{\tilde{\omega}} \approx \frac{-\alpha\varepsilon(\mathbf{r}_0)|\tilde{\mathbf{E}}(\mathbf{r}_0)|^2}{\iiint[\varepsilon|\tilde{\mathbf{E}}|^2 + \mu_0|\tilde{\mathbf{H}}|^2]\mathrm{d}^3\mathbf{r}} \equiv \frac{-\alpha}{2V(\mathbf{r}_0)}, \quad (1)$$

where $\varepsilon$ is the permittivity of the unperturbed cavity, $\varepsilon_0$ and $\mu_0$ are vacuum permittivity and permeability, and $\tilde{\mathbf{E}}$ and $\tilde{\mathbf{H}}$ are the unperturbed-cavity-mode electric and magnetic fields. The seminal Eq. (1) has been initially proposed by Bethe and Schwinger in optics [1] and Waldron in the radio-frequency domain [2,3] and has been used in similar variants until recently [3–7]. For convenience, we have introduced the mode volume ($V$), the classical *real* quantity used throughout in quantum electrodynamics [8,9] that gauges the coupling of an emitting dipole with the cavity mode. $V$ is usually defined for dipoles placed at the field-intensity maximum, where the coupling is also maximum. For convenience, we rather consider a spatially dependent mode $V$ to directly take into account the dependence of $\Delta\tilde{\omega}$ on the perturber position. Equation (1) has the merit of being intuitive and easy to evaluate, since $\Delta\tilde{\omega}$ solely depends on the unperturbed mode. It has been widely used for determining the dielectric and magnetic parameters of materials or testing the functionalities of microwave circuit components [3],

and, in the optical domain, to detect [10,11] or trap [7] nanoparticles, tune the resonance of photonic-crystal (PhC) cavities [4,12–17], analyze the impact of fabrication imperfections on these cavities [5], or study magnetic-like light–matter interactions [6,18]. Remarkably, Eq. (1) cannot accurately predict perturbation-induced changes of the quality factor ($Q$), $Q = -\frac{\text{Re}(\tilde{\omega})}{2\,\text{Im}(\tilde{\omega})}$. In particular, it predicts that changes in cavity loss rate follow the exact same spatial dependence as changes in the real frequency, with the sign of the polarizability setting the sign of the change in loss rate. This issue is known since the very beginning of perturbation theory and is sometimes accounted for by appending an additional flux-like term to Eq. (1) [3], even in recent works [17]. This term unfortunately requires solving the perturbed problem.

With the recent advent of theoretical results on the normalization of leaky resonator modes [8,19,20], it becomes evident that cavity perturbation theory cannot rely on normalization based on energy but on quasinormal-mode (QNM) formalism to account for the non-Hermitian character of the problem. Thus, it has been proposed recently that Eq. (1) is conveniently replaced by

$$\frac{\Delta\tilde{\omega}}{\tilde{\omega}} \approx \frac{-\alpha\varepsilon(\mathbf{r}_0)\tilde{\mathbf{E}}^2}{\iiint[\varepsilon\tilde{\mathbf{E}}^2 - \mu_0\tilde{\mathbf{H}}^2]\mathrm{d}^3\mathbf{r}} \equiv \frac{-\alpha}{2\tilde{V}(\mathbf{r}_0)}. \quad (2)$$

The sole difference between Eqs. (1) and (2) is the replacement of the *real* modal $V$ by a *complex* one $\tilde{V}$, which is calculated from the QNM-field distribution ($\tilde{\mathbf{E}}, \tilde{\mathbf{H}}$), see Section 2 in Supplement 1 for a more formal comparison. So far, only purely computational studies have been used to test the predictive force of Eq. (2), and those tests targeted highly non-Hermitian systems, i.e., low-$Q$ plasmonic nanoantennas [21] and metallic gratings [22].

Important open questions surround the proposed alternative perturbation formula, Eq. (2). For instance, even if it is evident that strongly non-Hermitian systems, like low-$Q$ plasmonics, require a revised perturbation theory, one wonders which genuine benefits, if any, can be expected from Eq. (2) for high-$Q$ microcavities, since these operate in a manner closely analogous to Hermitian systems with infinitesimal absorption or leakage [23]. More fundamentally, the question arises in QNM theory if the concept of complex mode $V$ introduced in Ref. [19] is just an abstract mathematical construct or if it carries true physical significance. In particular, the question of the physics captured by Im $\tilde{V}$ in Eq. (2) arises, for which simple intuitive arguments have not yet been presented in earlier works [21,22]. Finally, we note that no experiment has validated Eq. (2) so far. Even beyond the question whether this equation correctly captures real perturbation experiments, such an experiment could for the first time, to the best of our knowledge, test if QNMs, which are widely regarded as difficult mathematical objects with complex frequencies and divergent fields, are, in fact, directly measurable physical objects that can be mapped through unique signatures in experiments.

This work answers all three questions. In particular, we provide experimental evidence that the perturbation theory of high-$Q$ microcavities, like low-$Q$ resonators, should rely on non-Hermitian physics. Second, as a direct consequence of the relation between $\Delta \tilde{\omega}$ and $\tilde{V}$ in Eq. (2), we show that our perturbation measurements of $\Delta \tilde{\omega}$ allow for a direct mapping of the spatial distribution of $\tilde{V}$. This is an important result since $\tilde{V}$ is rooted into the local density of electromagnetic states (LDOS) of resonators and thus deeply involved in important phenomena of light–matter interactions in non-Hermitian open systems, e.g., the Purcell effect and strong coupling [8]. We also conclusively clarify the physics captured by Im $\tilde{V}$. Finally, we provide the first, to the best of our knowledge, analysis of the validity domain of Eq. (2), pinpointing the physics that causes the breakdown of even the revised perturbation theory.

Our main experimental results, obtained for a PhC cavity formed by four missing holes organized in a hexagonal array of holes, are summarized in Fig. 1. Electron beam lithography followed by reactive ion etching is used to fabricate the perforated GaAs membrane in air [15]. InAs quantum dots emitting at 1300 nm and excited at 780 nm are embedded in the GaAs membrane. We use a commercial scanning near-field optical microscope (SNOM) from TwinSNOM-Omicron in illumination/collection configuration. The fiber tip, a chemically etched, uncoated near-field fiber probe [15], plays the role of the perturber and the probe. It is raster scanned at a constant height above the membrane surface, and, for each position, we record the fluorescence spectrum from Q-dots, see Supplement 1 for details. By fitting the recorded lineshape with a Lorentzian profile, we infer the resonance wavelength and the Q. Three spectra recorded for three tip positions, labeled A, B, and C in Fig. 1(a), are plotted in Fig. 1(c). The perturbation is dominantly localized at the tip apex, while the fluorescence intensity is collected at the apex and along the tip sides (the intensity only decreases by a factor of 2 between $z = 0$ and $z = 300$ nm). Then, we can finely tune the perturbation position, while maintaining a nearly constant signal-to-noise ratio of the fluorescence measurements.

The results, shown with the resonance-shift map in Fig. 1(b), are in quantitative agreement with previous reports [4,14,15,24] showing resonance red shifts with tiny dielectric perturbers.
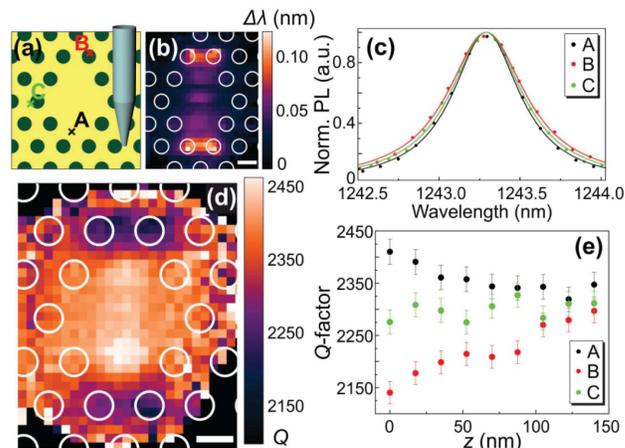


**Fig. 1.** Experimental results. (a) Sketch of the PhC cavity. (b) Wavelength-shift map as the tip is scanned over the cavity, with superimposed holes. (c) Photoluminescence recorded for three tip positions, A, B, and C shown in (a). Curves are Lorentzian fits of the data small points. The black and red points are blue-shifted by 0.05 and 0.08 nm to ease the visual comparison for cavity $Q$'s. (d) Perturbation-induced $Q$ map. (e) $Q$ as a function of the offset distance $z - d_{min}$ between the tip and the PhC membrane. Conclusively, the same tip may either enhance or decrease the intrinsic $Q = 2300 \pm 40$, depending on its position. The PhC parameters are lattice period $a = 331$ nm, hole diameter $\approx 206$ nm, and GaAs-membrane thickness 320 nm.

We estimate that the spatial resolution, which defines the dimension of the tip perturbation, is $\approx 70$ nm. More important in the present context are the tip-induced variations of $Q$, whose map in Fig. 1(d) shows both $Q$ increases and $Q$ decreases for the first time, to the best of our knowledge [25]. In order to link all these values to the intrinsic cavity $Q$ (without perturber), we additionally repeat the SNOM scans for different tip distances $d$ with respect to the membrane interface. Note that the minimum separation distance, $d_{min} \approx 30$ nm, depends on the tip–interface interaction and cannot be accurately measured. The data recorded for the three tip positions are given in Fig. 1(e). The three series of data all tend to $Q = 2300 \pm 40$, which is also the intrinsic $Q$ value measured when the tip is 1 μm away from the sample. An important and simple outcome of Figs. 1(c)–1(e) is that the *same* perturber may either increase $Q$ (point A), leave $Q$ unchanged (point C), or decrease $Q$ (point B). Therefore, our hyperspectral mapping of the of the QNM near-field refutes the general validity of Eq. (1). Further analysis of the experimental $\Delta \tilde{\omega}$ map will be provided afterwards.

To quantitatively test Eq. (2) for high-$Q$ cavities and quantify its domain of validity, we consider the same geometry and material as in the experiment (the membrane refractive index is assumed to be 3.46) and replace the tip by a deep-subwavelength dielectric perturber (volume $V_p$, permittivity $\Delta \varepsilon + \varepsilon_b$ with $\varepsilon_b \equiv \varepsilon(\mathbf{r}_0)$). We compute the resonance mode of the unperturbed cavity with the QNM solver QNMEig [26,27] implemented in COMSOL Multiphysics [28]. QNMEig provides normalized QNMs [$\tilde{\mathbf{E}}, \tilde{\mathbf{H}}$], with $\iiint (\varepsilon \tilde{\mathbf{E}}^2 - \mu_0 \tilde{\mathbf{H}}^2) d^3 \mathbf{r} = 1$, and $\tilde{V}(\mathbf{r}_0)$ is simply given by $(2\varepsilon(\mathbf{r}_0) \tilde{\mathbf{E}}^2 (\mathbf{r}_0))^{-1}$. The computed eigenfrequency is $\tilde{\lambda} = 2\pi c / \tilde{\omega} = 1364 + i 0.13$ nm, implying that the computed $Q$ is two times larger than the experimental one, probably because of losses induced by layer absorption, surface roughness, or other extrinsic
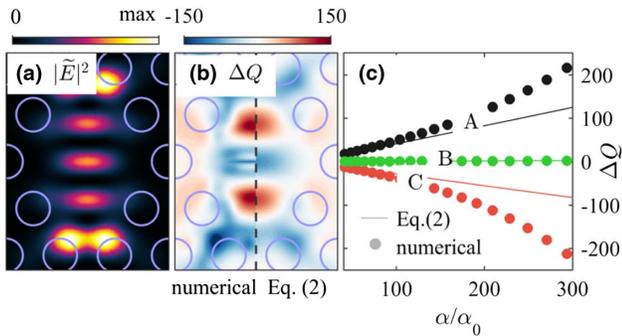
effects. A spatial map of $|\tilde{\mathbf{E}}|^2$ in a plane 30 nm above the cavity surface is shown in Fig. 2(a).

Figure 2(b) compares the change in $Q$, $\Delta Q$'s predicted with Eq. (2) with exact values computed by solving for the perturbed cavity. The data are obtained for a dipole polarizability $\alpha = 4\pi R^3 \frac{\varepsilon_{SiO_2}/\varepsilon_0 - 1}{\varepsilon_{SiO_2}/\varepsilon_0 + 2}$, corresponding to the static polarizability of a silica ($\varepsilon_{SiO_2} = 2.25\varepsilon_0$) nanosphere in air of radius $R = 55$ nm. Since we use exactly the same mesh for the two computations, numerical dispersion is negligible, and the comparison strictly quantifies the error due to the single-mode approximation. Figure 2(c) compares the $\Delta Q$ predictions of Eq. (2) with exact numerical values for increasing values of the perturber polarizability $\alpha$, which is assumed to be real. Three perturber locations, corresponding to the three tip positions used in the experiment, are considered. Remarkably, our key experimental observation that the same perturber may either decrease or increase $Q$ as its position is varied, independently of the wavelength-shift sign, is well captured by Eq. (2).

As expected, Fig. 2(c) evidences that for vanishing $\alpha$'s, Eq. (2) is virtually exact. However, some differences, not observed in previous studies for low-$Q$ plasmonic structures [21,22], are observed for $\alpha > 150\alpha_0$. This leads us to the important question of the conditions under which Eq. (2) may be used with confidence, and what parameters are impacting its domain of validity. For clarification, let us briefly recall the approximations needed to derive the perturbation formula. We focus on perturbations so small that the point-dipole approximation applies, in which case the perturber acts as an induced dipole moment $\mathbf{p}\delta(\mathbf{r} - \mathbf{r}_0)$. The total incident field driving the dipole is the sum of the external field $\mathbf{E}_b(\mathbf{r}_0, \omega)$ and the field scattered by the cavity onto the dipole,

$$\mathbf{p} = \alpha(\omega)\{\mathbf{E}_b + \mu_0\omega^2\Delta\mathbf{G}(\mathbf{r}_0, \mathbf{r}_0, \omega)\mathbf{p}\}, \qquad (3)$$

where the polarizability $\boldsymbol{\alpha}(\omega) = \alpha(\omega)\mathbf{I}$ is a diagonal tensor with all elements being equal [29] and defined for a perturber placed in an homogenous medium of permittivity of permittivity $\varepsilon(\mathbf{r}_0, \omega)$, $\Delta\mathbf{G}$



is a regularized scattering tensor [30] satisfying $\mathbf{G} = \mathbf{G_0} + \Delta\mathbf{G}$, with $\mathbf{G}(r_0, r, \omega)$ and $\mathbf{G_0}$ the Green tensors of the unperturbed cavity and of the uniform medium of permittivity $\varepsilon(r_0, \omega)$, respectively. $\Delta\mathbf{G}$ encompasses both the coupling to the unperturbed mode of interest and to all the other cavity modes, and accordingly, is expressed as [8]

$$\Delta\mathbf{G}(\mathbf{r}, \mathbf{r}', \omega) = \frac{-\tilde{\omega}\tilde{\mathbf{E}}_N(\mathbf{r}) \otimes \tilde{\mathbf{E}}_N(\mathbf{r}')}{\mu_0\omega^2(\omega - \tilde{\omega})} + \delta\mathbf{G}(\mathbf{r}, \mathbf{r}', \omega), \qquad (4)$$

where the first term represents the contribution from the non-degenerated (and normalized, see below) mode $\tilde{\mathbf{E}}_N(\mathbf{r})$ of interest, while the second term gathers the contribution of all other cavity modes and a continuum of radiation modes for cavities located in non-uniform backgrounds, on substrates for instance [26,27]. Full analyticity is recovered by neglecting the $\delta\mathbf{G}$ term in Eq. (4). Doing so and injecting Eq. (3) into Eq. (4) in the absence of the external field $\mathbf{E}_b(\mathbf{r}_0, \omega)$, we directly obtain Eq. (2).

In Supplement 1, we analyze the impact of omitting $\delta\mathbf{G}$. Since both terms in the right-hand side of Eq. (4) depend on the perturber position differently, we have to make several approximations. We assume real values for the polarizability $\alpha$ and neglect the vectorial character of the coupling, approximating $\delta\mathbf{G}$ by a diagonal tensor with identical diagonal terms $\delta G$ equal to one third of the trace of $\delta\mathbf{G}$. This way, we find two upper bounds for $\alpha$ to obtain accurate predictions of $\Delta\tilde{\omega}$ with Eq. (2). For $\mathrm{Re}\,\Delta\tilde{\omega}$, $\alpha < \alpha_r \equiv |\frac{1}{\mu_0\mathrm{Re}(\tilde{\omega}^2\delta G)}|$, and, for $\mathrm{Im}\,\Delta\tilde{\omega}$, two conditions have to be satisfied, $\alpha < \alpha_r$ and $\alpha < \alpha_i \equiv |\frac{1}{\mu_0\mathrm{Im}(\tilde{\omega}^2\delta G)}|\,|\frac{\mathrm{Im}\,\tilde{V}^{-1}}{\mathrm{Re}\,\tilde{V}^{-1}}|$, implying that $\mathrm{Im}(\Delta\tilde{\omega})$, i.e., $\Delta Q$, can be predicted, at best, with the same accuracy as $\Delta\lambda$, but not better. Moreover, as $Q$ increases, $|\frac{\mathrm{Im}\,\tilde{V}^{-1}}{\mathrm{Re}\,\tilde{V}^{-1}}|$ decreases towards zero, and so does $\alpha_i$. Therefore, it is more difficult to predict $\Delta Q$ accurately for a high-$Q$ cavity than for a low-$Q$ one. This explains why no visible deviation between the predictions of Eq. (2) and exact numerical data have been detected in earlier works on plasmonic nanoresonators, even for large shell perturbers [21,22]. Finally, for our present cavity, strong near-field interactions between the perturber and the PhC membrane result in $|\mathrm{Re}\,\delta G| \gg |\mathrm{Im}\,\delta G|$ for all perturber positions (see Supplement 1 for specific numerical values). This explains why the predictions of $\Delta Q$ in Fig. 2(c) and those of $\Delta\lambda$ in Fig. S4 in Supplement 1 are equally accurate over the entire range of polarizability values.

The success of Eq. (2) to predict $Q$-changes resides in the replacement of a real mode $V$ by a complex one, and, more precisely, of $|\tilde{\mathbf{E}}(\mathbf{r}_0)|^2$ by $\tilde{\mathbf{E}}^2(\mathbf{r}_0)$ in the denominator of $\tilde{V}$. This replacement preserves the phase information $\phi(\mathbf{r}_0)$ of the mode at the perturber location. For an intuitive picture that explains why the phase is essential, consider a driving field impinging onto a perturbed cavity. The field does not see the tiny perturber and at first instance excites the cavity as if it were unperturbed. The cavity then directly scatters in free space and also excites the perturber, which in turn re-excites the cavity mode with a round-trip dephasing delay of $2\phi(\mathbf{r}_0)$. The total radiated field by the cavity results from the interference of the direct initial radiation and the delayed one. Depending on whether these interferences are constructive or destructive, the total cavity radiation can be higher or lower than the intrinsic cavity radiation, possibly allowing for either an increase or a decrease of $Q$. This *a posteriori* explains why Eq. (1) which relies on an $\tilde{\mathbf{E}} \cdot \tilde{\mathbf{E}}^*$ product and, hence, losing the phase information, fails to predict $Q$-changes.

**Fig. 2.** Numerical test of Eq. (2) for the cavity used in the experiment. (a) Maps of $|\tilde{\mathbf{E}}|^2$. (b) Comparison between the $\Delta Q$ maps predicted with Eq. (2) (left) and exact values (right) for $\alpha = 166\alpha_0$. (c) Validity of Eq. (2) for increasing values of the polarizability and for the three tip positions, A, B, and C, used in the experiment. $\alpha_0$ denotes the static polarizability of a 10-nm-radius silica sphere in air, so that the full horizontal scale covers silica spheres with radii from 10 to 70 nm. Note that Eq. (1) predicts $\Delta Q = 0$ for all positions and all $\alpha$. In (b) and (c), the point-dipole perturber is assumed to be located in a plane 30 nm above the semiconductor PhC membrane, and the exact values are computed by iteratively searching the complex-frequency pole of Eq. (4) for $\mathbf{E}_b = 0$ with the regularized scattering tensor $\Delta\mathbf{G}(\mathbf{r}, \mathbf{r}', \omega)$ computed with COMSOL Multiphysics [27].
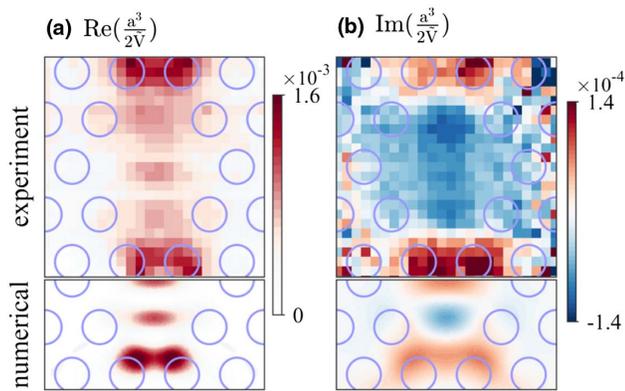
**(a)** $\mathrm{Re}\left(\frac{a^3}{2\tilde{V}}\right)$  **(b)** $\mathrm{Im}\left(\frac{a^3}{2\tilde{V}}\right)$



**Fig. 3.** Maps of (a) $\mathrm{Re}(\tilde{V}^{-1})$ and (b) $\mathrm{Im}(\tilde{V}^{-1})$ computed with the QNM solver 30 nm above the semiconductor membrane (bottom) and directly inferred from the $\Delta\tilde{\omega}$ measurements using Eq. (2) with a tip polarizability $\alpha_{\mathrm{tip}} = 166\alpha_0$ (top). Note that the experimental values are all rescaled by a factor of ¼.

The concept of complex $\tilde{V}'s$ is recent [19]. It seems to be rooted in important phenomena of light–matter interactions in non-Hermitian open systems [8]. For instance, the ratio $\mathrm{Im}\,\tilde{V}^{-1}/\mathrm{Re}\,\tilde{V}^{-1}$ quantifies the spectral asymmetry of the mode contribution (or LDOS) to the modification of the spontaneous emission rate of an emitter weakly coupled to a cavity [19]. For strong coupling, it modifies the usual expression of the Rabi frequency [9] by blurring and moving the boundary between the weak and strong coupling regimes [8,31]. Despite these strong roots, complex $\tilde{V}'s$ are often seen as a mathematical abstraction. In fact, Eq. (2) and our experiment show that complex $\tilde{V}'s$ are not just a mathematical tool, but, in fact, are directly measurable.

Figure 3 shows the maps of $\mathrm{Re}\,\tilde{V}^{-1}$ and $\mathrm{Im}\,\tilde{V}^{-1}$, which have been directly inferred from our $\Delta\tilde{\omega}$ measurements by injecting a tip polarizability $\alpha_{\mathrm{tip}} = 166\alpha_0$ (tip curvature radius of $R = 55$ nm) in Eq. (2). For comparison, we also plot the theoretical maps computed with the QNM solver. Note that to allow for a better comparison, we have multiplied the experimental values of $\mathrm{Re}\,\tilde{V}^{-1}$ and $\mathrm{Im}\,\tilde{V}^{-1}$ by a 1/4 rescaling factor. The latter corresponds to a tip radius only 30% larger ($R = 73$ nm) and can be understood by considering that a static sphere dipolar polarizability is a simplistic model for the tip used in our experiment. There are differences between the experimental maps and the computed ones. Nevertheless, the experimental and theoretical maps qualitatively share the same dominant features, notably a successful agreement on the *locations* and *amplitudes* of the minimum and maximum values, and an overall 10 fold difference between $\mathrm{Re}\,\tilde{V}^{-1}$ and $\mathrm{Im}\,\tilde{V}^{-1}$.

To summarize, we have demonstrated, with hyperspectral-imaging near-field experiments, that the perturbation theory of high-$Q$ microcavities should rely on complex modal Vs to fully account for the role of the perturber at the nanoscale. This demonstration is a first, to the best of our knowledge, and direct evidence of the effects of complex modal Vs, arising from the intrinsic property of all photonic resonators of being an open (i.e., non-Hermitian) system, on the optical response of a photonic system. We have shown that QNM theory allows for a quantitative prediction of both $\mathrm{Re}(\Delta\tilde{\omega})$ and $\mathrm{Im}(\Delta\tilde{\omega})$ as a function of the perturber position, whereas the classical theory based on Hermitian physics only gives access to $\mathrm{Re}(\Delta\tilde{\omega})$. Equation (2) combines great simplicity and predictive power. It may find applications in

various problems related to sensing or trapping, as the additional information provided by dual maps may help lift the degeneracy of single $\Delta\lambda$-maps, for instance, allowing not only the detection of a binding event in sensing but also the binding location [11]. Other perspectives concern the analysis of the impact of fabrication imperfections on $Q$'s, post-fabrication $Q$-control [12], optimization of cavities with large $Q$'s, or inverse design of cavities with tailored $\Delta\lambda$ and $\Delta Q$ maps. Equation (2) also offers the possibility to perform direct measurement of the complex mode $V$ of microcavities, giving greater visibility and operational capacity to an important physical quantity of resonant light–matter interactions.

See Supplement 1 for supporting content.

## REFERENCES AND NOTES

1. H. A. Bethe and J. Schwinger, "Perturbation theory for cavities," N.D.R.C. Rpt. D1-117 (Cornell University, 1943).
2. R. A. Waldron, "Perturbation theory of resonant cavities," Proc. IEEE **107**, 272–274 (1960).
3. O. Klein, D. M. Dressel, and G. Grüner, "Microwave cavity perturbation techniques: part I: principles," Int. J. Infrared Millim. Waves **14**, 2423–2457 (1993).
4. L. Lalouat, B. Cluzel, P. Velha, E. Picard, D. Peyrade, J. P. Hugonin, P. Lalanne, E. Hadji, and F. De Fornel, "Near-field interactions between a subwavelength tip and a small-volume photonic-crystal nanocavity," Phys. Rev. B **76**, 041102 (2007).
5. L. Ramunno and S. Hughes, "Disorder-induced resonance shifts in high-index-contrast photonic crystal nanocavities," Phys. Rev. B **79**, 161303 (2009).
6. M. Burresi, T. Kampfrath, D. van Oosten, J. C. Prangsma, B. S. Song, S. Noda, and L. Kuipers, "Magnetic light-matter interactions in a photonic crystal nanocavity," Phys. Rev. Lett. **105**, 123901 (2010).
7. L. Neumeier, R. Quidant, and D. E. Chang, "Self-induced back-action optical trapping in nanophotonic systems," New J. Phys. **17**, 123008 (2015).
8. P. Lalanne, W. Yan, K. Vynck, C. Sauvan, and J.-P. Hugonin, "Light interaction with photonic and plasmonic resonances," Laser Photon. Rev. **12**, 1700113 (2018).
9. J.-M. Gérard, "Solid-state cavity-quantum electrodynamics with self-assembled quantum dots," in *Single Quantum Dots*, Topics in Applied Physics (2003), Vol. **90**, p. 269.
10. F. Vollmer and S. Arnold, "Whispering-gallery-mode biosensing: label-free detection down to single molecules," Nat. Methods **5**, 591–596 (2008).
11. K. D. Heylman, K. A. Knapper, E. H. Horak, M. T. Rea, S. K. Vanga, and R. H. Goldsmith, "Optical microresonators for sensing and transduction: a materials perspective," Adv. Mater. **29**, 1700037 (2017).
12. A. Badolato, K. Hennessy, M. Atatüre, J. Dreiser, E. Hu, P. M. Petroff, and A. Imamoğlu, "Deterministic coupling of single quantum dots to single nanocavity modes," Science **308**, 1158–1161 (2005).

13. A. F. Koenderink, M. Kafesaki, B. C. Buchler, and V. Sandoghdar, "Controlling the resonance of a photonic crystal microcavity by a near-field probe," Phys. Rev. Lett. **95**, 153904 (2005).

14. S. Mujumdar, A. F. Koenderink, T. Sünner, B. C. Buchler, M. Kamp, A. Forchel, and V. Sandoghdar, "Near-field imaging and frequency tuning of a high-Q photonic crystal membrane microcavity," Opt. Express **15**, 17214–17220 (2007).

15. F. Intonti, S. Vignolini, F. Riboli, A. Vinattieri, D. S. Wiersma, M. Colocci, L. Balet, C. Monat, C. Zinoni, L. H. Li, R. Houdré, M. Francardi, A. Gerardino, A. Fiore, and M. Gurioli, "Spectral tuning and near-field imaging of photonic crystal microcavities," Phys. Rev. B **78**, 041401 (2008).

16. N. Le Thomas and R. Houdré, "Inhibited emission of electromagnetic modes confined in subwavelength cavities," Phys. Rev. B **84**, 035320 (2011).

17. F. Ruesink, H. M. Doeleman, R. Hendrikx, A. F. Koenderink, and E. Verhagen, "Perturbing open cavities: anomalous resonance frequency shifts in a hybrid cavity-nanoantenna system," Phys. Rev. Lett. **115**, 203904 (2015).

18. S. Vignolini, F. Intonti, F. Riboli, L. Balet, L. H. Li, M. Francardi, A. Gerardino, A. Fiore, D. S. Wiersma, and M. Gurioli, "Magnetic imaging in photonic crystal microcavities," Phys. Rev. Lett. **105**, 123902 (2010).

19. C. Sauvan, J. P. Hugonin, I. S. Maksymov, and P. Lalanne, "Theory of the spontaneous optical emission of nanosize photonic and plasmon resonators," Phys. Rev. Lett. **110**, 237401 (2013).

20. E. A. Muljarov and W. Langbein, "Resonant-state expansion of dispersive optical open systems: creating gold from sand," Phys. Rev. B **93**, 075417 (2016).

21. J. Yang, H. Giessen, and P. Lalanne, "Simple analytical expression for the peak-frequency shifts of plasmonic resonances for sensing," Nano Lett. **15**, 3439 (2015).

22. T. Weiss, M. Mesch, M. Schäferling, H. Giessen, W. Langbein, and E. A. Muljarov, "From dark to bright: first-order perturbation theory with analytical mode normalization for plasmonic nanoantenna arrays applied to refractive index sensing," Phys. Rev. Lett. **116**, 237401 (2016).

23. A. Oskooi and S. G. Johnson, "Electromagnetic wave source conditions," in *Advances in FDTD Computational Electrodynamics: Photonics and Nanotechnology*, A. Taflove, A. Oskooi, and S. G. Johnson, eds. (Artech House, 2013), Chap. 4.

24. N. Caselli, F. Intonti, F. La China, F. Riboli, A. Gerardino, W. Bao, A. W. Bargioni, L. Li, E. H. Linfield, F. Pagliano, A. Fiore, and M. Gurioli, "Ultra-subwavelength phase-sensitive Fano-imaging of localized photonic modes," Light Sci. Appl. **4**, e326 (2015).

25. $Q$-increases by modifying cavity geometry have been previously reported using slabs [16] and scatterer gratings [17] in near-fields, but not with a localized perturbation, nor with scanning through the mode to determine the relation between changes and mode distributions. Perturbations by extended structures, like slabs, have been understood as radiation pattern engineering to control.

26. W. Yan, R. Faggiani, and P. Lalanne, "Rigorous modal analysis of plasmonic nanoresonators," Phys. Rev. B **97**, 205422 (2018).

27. QNMEig and companion Matlab Toolboxes are available on the webpage of L. Lalanne.

28. https://www.comsol.com/ (Version 5.2a).

29. The present theory is derived for isotropic and non-magnetic perturbers for the sake of simplicity, but these assumptions can be easily removed.

30. L. Novotny and B. Hecht, *Principles of Nano-Optics* (Cambridge University, 2006), Chap. 15.

31. E. Lassale, N. Bonod, T. Durt, and B. Stout, "Interplay between spontaneous decay rates and Lamb shifts in open photonic systems," Opt. Lett. **43**, 1950–1953 (2018).